




Kiyan Musaie,<sup>a</sup> Samin Abbaszadeh,<sup>b</sup> Vahideh Nosrati-Siahmazgi,<sup>a</sup> Mostafa Qahremani,<sup>a</sup> Shige Wang,<sup>c</sup> Mohammad Reza Eskandari,<sup>d</sup> Seyyed Vahid Niknezhad,<sup>e</sup> Fakhri Haghi,<sup>f</sup> Yulin Li, <sup>g</sup> Bo Xiao <sup>\*h</sup> and Mohammad-Ali Shahbazi <sup>\*a,i,j</sup>

Received 30th November 2022,  
Accepted 4th February 2023

DOI: 10.1039/d2bm01965e

[rsc.li/biomaterials-science](http://rsc.li/biomaterials-science)

Therapeutics against breast cancer have undergone long-term development, yet only surgery, chemotherapy, and radiotherapy are widely used in the clinic.<sup>1–4</sup> Unfortunately, these approaches are not efficient enough for completely curing cancer, and still 15.5% of cancer-related deaths in females

have been reported to be due to breast tumors in 2020.<sup>5,6</sup> Even combining surgery, as the major form of a treatment strategy for breast cancer, with chemotherapy is not an ideal approach, due to the poor drug accumulation in the tumor tissue, leading to low therapeutic effects, causing serious damage to healthy organs, and drug resistance as well as high risk of local recurrence (10% to 41%) due to the failure of surgery to eliminate all

† Electronic supplementary information (ESI) available: Experimental section. See DOI: <https://doi.org/10.1039/d2bm01965e>

tumor cells at the edges of the surgery site.<sup>7–9</sup> Moreover, the unsatisfactory postsurgical physiological condition of patients would delay the healing of the created wound due to inflammation and potential bacterial infection.<sup>10,11</sup>

Currently, there is no clinically relevant formulation in the market with multifunctional properties to simultaneously settle the problems of complete eradication of tumor cells from the site of surgery, bacterial infections, and subsequent wounds to increase the survival rate and life quality of patients. However, tremendous advances in nanotechnology and biomaterials have enabled the possibility of proposing new strategies for combined therapy and regeneration by nano-incorporated hydrogels.<sup>12–14</sup> For example, injectable hydrogels, constructed through dynamic crosslinks, have been widely applied for direct injection into the cancer tissue and sustained drug release through prolonged maintenance of the hydrogel in the target site. In recent years, a number of natural polymers have been used to prepare injectable hydrogels.<sup>15,16</sup> Farsi gum (FG) is an exudate polysaccharide obtained from the trunk and branches of *Amygdalus scoparia* Spach, which is less studied despite its high potential for biomedical application due to its low-cost, safety, and high-water absorption.<sup>17–22</sup> Sodium alginate (Alg), an anionic polysaccharide, is another widely used natural polymer for the preparation of hydrogels due to its biocompatibility, low toxicity, and facile gel formation ability.<sup>23,24</sup> Interestingly, these two polymers can present an enhanced hemostatic capacity through their high-water absorbing capacity and negative charge, which can induce coagulation by initiating the autoactivation of the coagulation factor XII.<sup>25,26</sup> In addition, injectable hydrogels can be formed from these two polymers by facile crosslinking approaches like metal coordination,<sup>27,28</sup> which renders the merits of easy operation, avoidance of chemical modification for hydrogel formation, and effective delivery of chemotherapeutics for cancer therapy.

As an alternative to chemotherapy, photothermal therapy (PTT) has attracted considerable attention due to its minimal invasiveness and selectivity for the localized ablation of tumor cells by light-to-heat conversion upon near-infrared (NIR) irradiation without significant damage to other organs.<sup>29–31</sup> PTT over 50 °C in the tumor tissues can effectively induce cancer cell necrosis.<sup>32</sup> However, the heat generated from PTT still causes local tissue lesions and subsequent bacterial infections might occur in the NIR-irradiated site.<sup>33,34</sup> To overcome the challenge of delayed wound repair after high-temperature PTT, various strategies, such as the use of anti-inflammatory,<sup>35,36</sup> angiogenic,<sup>37–40</sup> and extracellular matrix mimicking<sup>41,42</sup> hydrogels can be employed. However, photoactive nanomaterials that are loaded inside the hydrogels for cancer PTT can be used to locally enhance the temperature to 40 °C for the acceleration of tissue regeneration by the thermal induction of cell proliferation and angiogenesis.<sup>43,44</sup> This concept allows combined cancer therapy and tissue regeneration using a single injectable hydrogel by the adjustment of laser power to control the temperature in therapy and regenerative phases. In addition, PTT can lead to irreversible mem-

brane destruction of bacterial cells and reduce the risk of infection.<sup>45</sup>

Currently, numerous PTT agents have been loaded into hydrogels for cancer therapy, such as graphene,<sup>46</sup> gold nanostructures,<sup>47</sup> carbon dots,<sup>48</sup> and NIR-absorbing organic dyes.<sup>49</sup> Bi<sub>2</sub>S<sub>3</sub> nanorods (NRs) are also novel photothermal agents with excellent photothermal conversion efficiency, facile fabrication, and favorable biocompatibility.<sup>12,50–52</sup> Additionally, the surface of these particles can be easily modified by targeting agents to endow them with a high affinity to tumor cells and increase their maintenance in the tumor tissue for a long time after the injection of hydrogels.<sup>53,54</sup> Meanwhile, the intrinsic antibacterial effect of Bi<sub>2</sub>S<sub>3</sub> particles can prevent microbial infection after cancer therapy.<sup>55,56</sup>

Herein, as shown in Fig. 1a, hyaluronic acid-coated Bi<sub>2</sub>S<sub>3</sub> (BiH) NRs were synthesized as a photothermally active nanomaterial, which presented a good photothermal performance in the tumor bed. In addition, an injectable hydrogel was formed by the Fe<sup>3+</sup>-mediated coordination of carboxyl and hydroxyl groups in Alg and hydroxyl groups in FG, providing dynamic bonds that can reversibly break and reform to achieve self-healing properties (Fig. 1b).<sup>57–61</sup> The BiH and allantoin (Alla) were co-loaded into the hydrogel to render combined photothermal cancer therapy and regenerative property to the hydrogel. Alla is a pharmaceutically active agent that can promote wound healing by regulating inflammatory reactions, stimulating fibroblast proliferation, and inducing extracellular matrix formation.<sup>62</sup> Furthermore, the local NIR-mediated temperature adjustment to 40 °C after cancer ablation can synergize the healing effect of Alla. In addition, the hydrogel represents antibacterial and hemostatic functions, which makes it a multifunctional platform for combined cancer therapy and regeneration (Fig. 1c).

## 2. Results & discussion

### 2.1. Physicochemical characterization of NRs

Physicochemical characterization studies of BiH NRs were carried out to ensure their successful preparation. Transmission electron microscopy (TEM) and field emission scanning electron microscopy (FE-SEM) imaging revealed that Bi<sub>2</sub>S<sub>3</sub> (Fig. S1a and S1b†) and BiH (Fig. 2a and b) NRs were rod-shaped with a tendency to agglomerate into flower-like microspheres. The surface zeta potential of Bi<sub>2</sub>S<sub>3</sub> NRs was  $-52.9 \pm 1.7$  mV, which changed to  $-15.1 \pm 1.7$  mV for BiH NRs (Fig. 2c). This observation confirms the successful coating of Bi<sub>2</sub>S<sub>3</sub> NRs with HA, which can cover negatively charged sulfur ions of the Bi<sub>2</sub>S<sub>3</sub> surface with its COO<sup>−</sup> groups, resulting in a substantially less negatively charged surface.<sup>63</sup> We noticed a higher colloidal stability and lower aggregation of BiH NRs in deionized water (DW) during 24 h of monitoring compared to those of Bi<sub>2</sub>S<sub>3</sub> due to the hydrophilic nature of HA (Fig. S2†). Furthermore, the Brunauer–Emmett–Teller (BET) analysis demonstrated a higher volume of N<sub>2</sub> adsorption ( $V_m$ ) and bigger values of surface area and total pore volume in BiH NRs



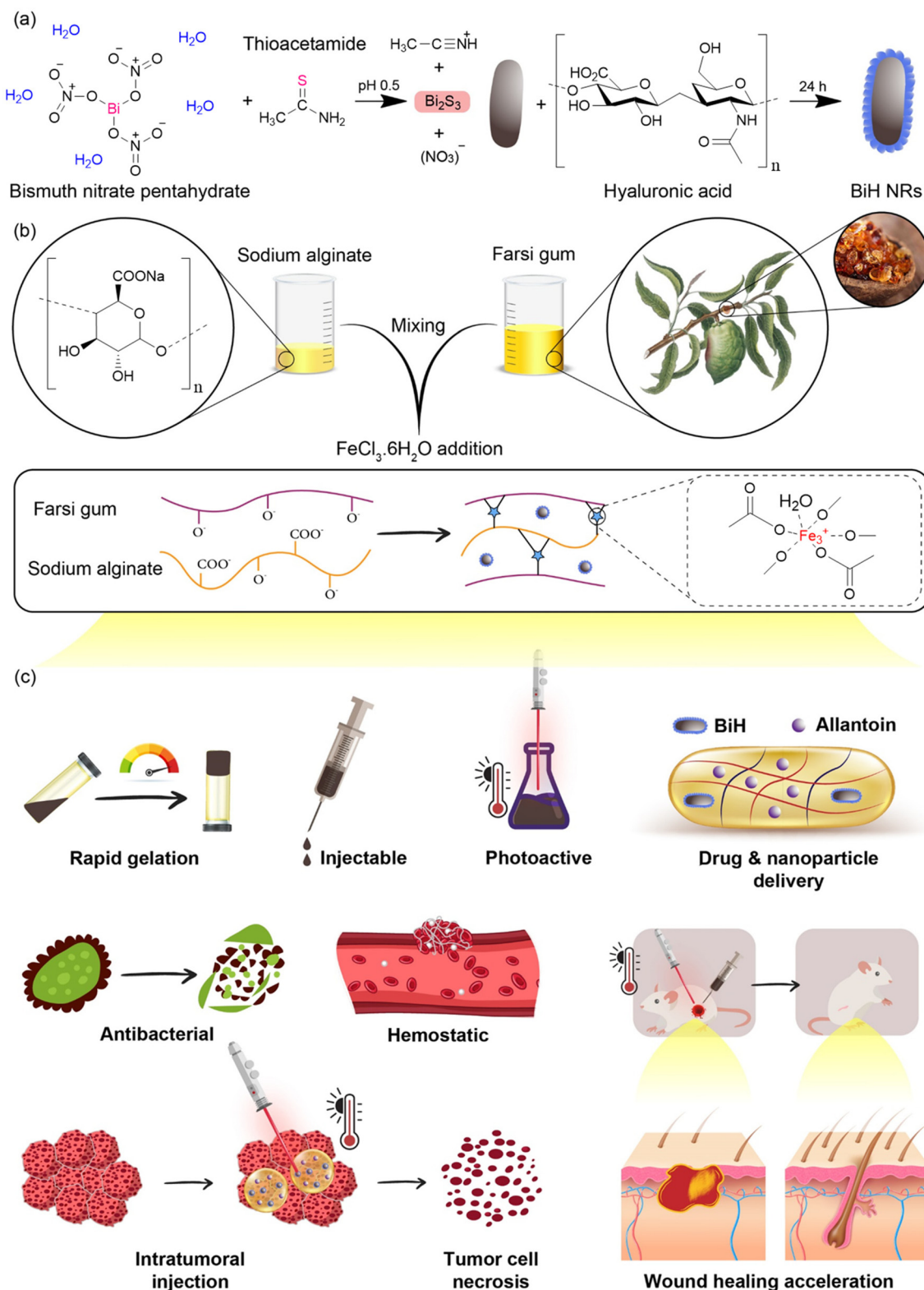


**Fig. 1** The schematic illustration for the preparation of BiH NRs, construction of metal-coordinated hydrogels, and their functions. (a)  $\text{Bi}_2\text{S}_3$  NRs were synthesized by a simple chemical reaction and further coated with HA. (b) The  $\text{Fe}^{3+}$ -coordinated hydrogel was achieved by posing functional groups of FG and Alg to  $\text{Fe}^{3+}$  ions. (c) Swiftly formed injectable Gel-BiH-Alla hydrogel showed the multifunctional mechanism of anti-infection, hemostatic effect, localized drug release, and NIR-triggered PTT effects for wound healing acceleration and anti-cancer therapy purposes.



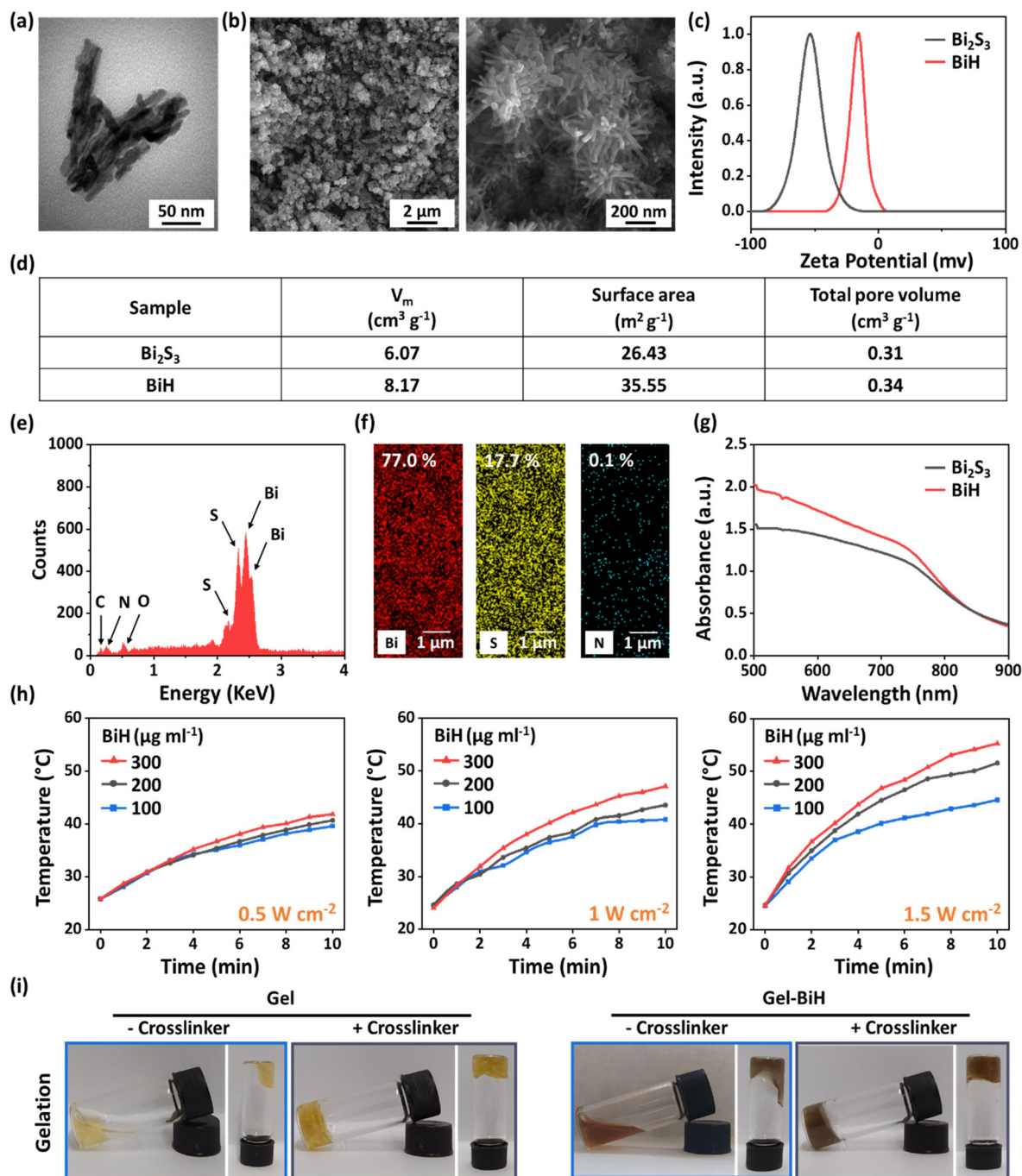


**Fig. 2** (a) The TEM image of BiH NRs. (b) FE-SEM images of BiH NRs at different magnifications. (c) The zeta potential of  $\text{Bi}_2\text{S}_3$  and BiH NRs. (d) BET analysis of  $\text{Bi}_2\text{S}_3$  and BiH NRs. (e and f) EDAX spectrum and elemental mapping of BiH NRs. (g) UV-vis absorption spectra of  $\text{Bi}_2\text{S}_3$  and BiH NRs. (h) Photothermal temperature curves of BiH NRs dispersed in DW at various concentrations of  $100 \mu\text{g ml}^{-1}$ ,  $200 \mu\text{g ml}^{-1}$ , and  $300 \mu\text{g ml}^{-1}$  under 808 nm laser irradiation with different power densities ( $0.5 \text{ W cm}^{-2}$ ,  $1 \text{ W cm}^{-2}$ , and  $1.5 \text{ W cm}^{-2}$ ) for 10 min. (i) Photographs of Gel and Gel-BiH hydrogels in the presence and absence of  $\text{FeCl}_3 \cdot 6\text{H}_2\text{O}$  as the crosslinker.

as compared to  $\text{Bi}_2\text{S}_3$  NRs due to the presence of HA chains on the surface of the NRs (Fig. 2d). Furthermore, the energy-dispersive X-ray spectroscopy (EDAX) analysis and elemental mapping of  $\text{Bi}_2\text{S}_3$  (Fig. S1c and S1d†) and BiH (Fig. 2e and f) NRs implied that the weight percentages of Bi and S decreased from 78.2% and 21.8% to 77.0% and 17.7%, respectively, after

HA coating.<sup>64</sup> We also found that O (1.1%) and N (0.1%) elements were present in BiH NRs, indicating the successful introduction of HA to the surface of  $\text{Bi}_2\text{S}_3$  NRs. In addition, UV-Vis spectra of both  $\text{Bi}_2\text{S}_3$  and BiH NRs showed an obvious absorption at 808 nm, indicating their potential to be photothermal agents (Fig. 2g).



The *in vitro* PTT evaluation of BiH NR suspensions (100  $\mu\text{g ml}^{-1}$ , 200  $\mu\text{g ml}^{-1}$ , and 300  $\mu\text{g ml}^{-1}$ ) showed a concentration-dependent temperature change at different power densities (0.5  $\text{W cm}^{-2}$ , 1  $\text{W cm}^{-2}$ , and 1.5  $\text{W cm}^{-2}$ ) under 808 nm laser irradiation over 10 min (Fig. 2h). In particular, after NIR irradiation (1.5  $\text{W cm}^{-2}$ , 10 min), the temperature values of BiH NR suspensions with concentrations of 100  $\mu\text{g ml}^{-1}$ , 200  $\mu\text{g ml}^{-1}$ , and 300  $\mu\text{g ml}^{-1}$  increased to 44.6  $^{\circ}\text{C}$ , 51.6  $^{\circ}\text{C}$ , and 55.3  $^{\circ}\text{C}$ , respectively. Since the suitable temperature for tumor eradication was reported to be around 50.0  $^{\circ}\text{C}$ ,<sup>65</sup> 200  $\mu\text{g ml}^{-1}$  of the BiH NR suspension with a power density of 1.5  $\text{W cm}^{-2}$  was selected for the subsequent anti-tumor investigations. Moreover, it was found that the temperature values of BiH NR suspensions with concentrations of 100  $\mu\text{g ml}^{-1}$ , 200  $\mu\text{g ml}^{-1}$ , and 300  $\mu\text{g ml}^{-1}$  increased to 40.8  $^{\circ}\text{C}$ , 43.5  $^{\circ}\text{C}$ , and 47.1  $^{\circ}\text{C}$ , respectively, under laser irradiation with a power density of 1  $\text{W cm}^{-2}$ . Considering that mild local heating (*ca.* 40–41  $^{\circ}\text{C}$ ) would be beneficial for cell proliferation, blood flow, and tissue regeneration,<sup>65</sup> 200  $\mu\text{g ml}^{-1}$  of the BiH NR suspension and an optimum laser power density of 1  $\text{W cm}^{-2}$  were chosen for wound healing studies.

## 2.2. Preparation and characterization of hydrogels

Metal-coordinated hydrogels were prepared using FG, Alg, and ferric chloride hexahydrate ( $\text{FeCl}_3 \cdot 6\text{H}_2\text{O}$ ). In fact, arabinose and galactose are the main components of FG polysaccharide,<sup>20</sup> and Alg as an anionic biomolecule brings up an extraordinary amount of negatively charged hydroxyl and carboxyl groups to the  $\text{Fe}^{3+}$  ions to form metal-coordinated bonds, which can induce immediate gel formation. Moreover, the Gel-BiH and Gel-BiH-Alla hydrogels were consequently formed by the addition of BiH NRs and Alla to the polymers before the crosslinking by  $\text{FeCl}_3 \cdot 6\text{H}_2\text{O}$  (the methodology is described in section 1.4 of the ESI†).

**2.2.1. Gelation time, porosity, initial water content, and yield.** The gelation process of hydrogels was studied with the tube inversion method (Fig. 2i). Initially, Gel and Gel-BiH were prepared without  $\text{FeCl}_3 \cdot 6\text{H}_2\text{O}$  as the cross-linker, and the flow of the solution indicated that hydrogels were not formed. With the addition of  $\text{FeCl}_3 \cdot 6\text{H}_2\text{O}$ , hydrogels were formed, and no flow was observed at the bottom-up position of the tubes. The gelation time was nearly 5 s after the addition of the cross-linker in the hydrogels with and without the loading of BiH NRs (Fig. S3a†), indicating that the presence of BiH NRs did not affect the formation of metal-coordination bonds among  $\text{Fe}^{3+}$  ions and hydroxyl/carboxyl groups of FG and Alg.

To evaluate the porosity structure of Gel, Gel-BiH, and Gel-BiH-Alla hydrogels, the liquid displacement method was exerted, and the porosity of all hydrogels was identified to be greater than 80.0% (Fig. S3b†). Meanwhile, BiH and Alla incorporation in the hydrogel matrix did not affect the high porosity of the Gel hydrogel, which can contribute to a desirable wound healing effect by good oxygen penetration and absorption of exudates.<sup>66</sup> In addition, the initial water contents (IWCs) of Gel and Gel-BiH hydrogels were  $79.2 \pm 1.7\%$  and  $80.7 \pm 2.5\%$ , respectively, confirming the high incorporation of

water inside the pores of the hydrogels (Fig. S4a†). The yields of Gel and Gel-BiH hydrogels were also calculated as  $87.6 \pm 8.9\%$  and  $77.0 \pm 4.9\%$ , respectively (Fig. S4b†). The IWC and yield data demonstrated that the incorporation of BiH in the hydrogel did not significantly affect these parameters.

**2.2.2. Fourier-transform infrared (FTIR) spectroscopy.** FTIR spectroscopy was conducted in the range of 4000–400  $\text{cm}^{-1}$  to characterize the structure of the pure ingredients, NRs, and prepared hydrogels (Fig. 3a). In the spectrum of FG, a band at 1041  $\text{cm}^{-1}$  was assigned to the C–O–C, C–CH, and C–OH stretching, and the bands at 646  $\text{cm}^{-1}$  and 783  $\text{cm}^{-1}$  corresponded to the C–H stretching.<sup>67</sup> Furthermore, the broad bands of the FG spectrum at 1577  $\text{cm}^{-1}$  and 1419  $\text{cm}^{-1}$  were assigned to the carboxyl groups. The bands at 2930  $\text{cm}^{-1}$  and 3422  $\text{cm}^{-1}$  were also related to asymmetric  $-\text{CH}_2-$  and  $-\text{OH}$  stretching, respectively.<sup>68</sup> In the spectrum of  $\text{FeCl}_3 \cdot 6\text{H}_2\text{O}$ , a band that appeared at 3371  $\text{cm}^{-1}$  was attributed to strong O–H stretching vibrations. Also, the band at 733  $\text{cm}^{-1}$  was assigned to the bending of the Fe–O bond.<sup>69</sup> In the spectrum of Alg, a band at 3440  $\text{cm}^{-1}$  was attributed to the O–H stretching, and the bands at 1576  $\text{cm}^{-1}$  and 1418  $\text{cm}^{-1}$  were assigned to the carboxyl groups.<sup>70</sup> Moreover, the band at 3422  $\text{cm}^{-1}$ , which is attributed to O–H stretching in the FG sample, was slightly shifted to 3425  $\text{cm}^{-1}$ , 3433  $\text{cm}^{-1}$ , 3433  $\text{cm}^{-1}$ , and 3439  $\text{cm}^{-1}$  for FG-Fe, Gel, Gel-BiH, and Gel-BiH-Alla samples, respectively, due to the successful formation of metal-coordinated bonds.

The successful synthesis of  $\text{Bi}_2\text{S}_3$  NRs was confirmed by the presence of the band at 1012  $\text{cm}^{-1}$ , assigned to the Bi–S bond.<sup>71</sup> A broad band at 3440  $\text{cm}^{-1}$  in the BiH spectrum was ascribed to the O–H groups in the structure of HA.<sup>72</sup> Additionally, the strong peak at 1580  $\text{cm}^{-1}$  referred to the C=O stretching vibration of the carboxyl group of HA, suggesting the successful coating of NRs. Due to the low concentration of BiH NRs within the hydrogel, the spectrum of Gel-BiH indicated no significant changes, in comparison with the Gel spectrum. FTIR spectrum of Alla showed asymmetric and symmetric vibrations of  $\text{NH}_2$  at 3441  $\text{cm}^{-1}$  and 3348  $\text{cm}^{-1}$ , respectively, and the C–H stretching vibration at 3063  $\text{cm}^{-1}$ .<sup>73</sup> All the mentioned bands were found in the Gel-BiH-Alla hydrogel, confirming the incorporation of Alla molecules inside the hydrogel matrix.

**2.2.3. XRD, TGA, and DTG studies.** X-ray diffraction analysis was used to evaluate the crystallinity of initial ingredients, NRs, and hydrogels as well as the interactions between components (Fig. 3b). X-Ray diffraction (XRD) evaluations of  $\text{FeCl}_3 \cdot 6\text{H}_2\text{O}$ ,  $\text{Bi}_2\text{S}_3$  NRs, BiH NRs, and Alla indicated their crystalline structures. It was observed that the broad characteristic peak at 20.61° for FG indicated a semi-crystalline microstructure.<sup>74</sup> The XRD pattern of Alg showed two characteristic broad diffraction peaks at 14.05° and 22.01°, indicating the semi-crystalline structure of Alg.<sup>75</sup> The XRD diffraction peak of FG shifted from 20.61° to 21.16°, 21.56°, 21.56°, and 22.56° in FG-Fe, Gel, Gel-BiH, and Gel-BiH-Alla hydrogels, respectively, indicating the formation of metal-coordination bonds.<sup>76</sup> While the XRD patterns of BiH were not observed in the Gel-BiH



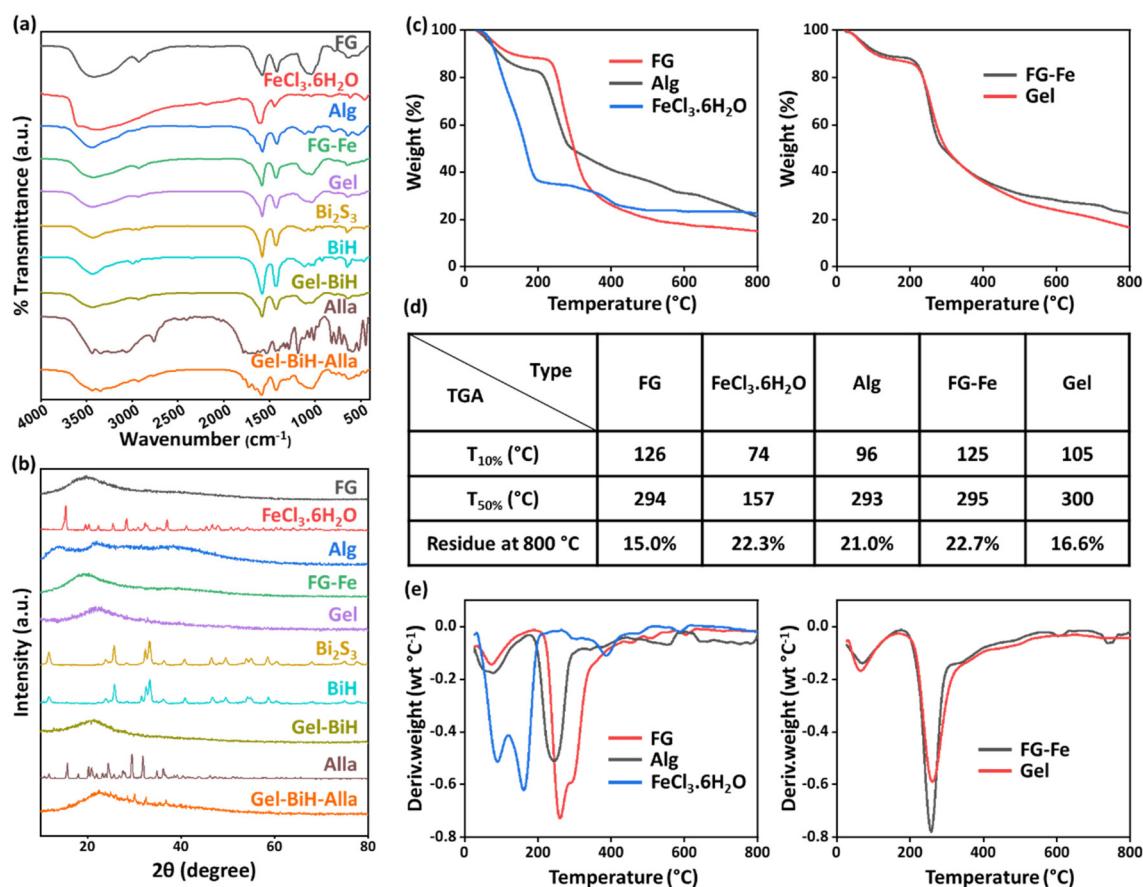


**Fig. 3** (a) FTIR spectra and (b) XRD profiles of pure components, NRs, and hydrogels. (c) TGA analysis of FG, Alg, FeCl<sub>3</sub>·6H<sub>2</sub>O, FG-Fe, and Gel samples. (d) The required temperature (°C) for 10% and 50% decomposition of each sample and the residual weight at 800 °C regained from TGA. (e) DTG analysis of FG, Alg, FeCl<sub>3</sub>·6H<sub>2</sub>O, FG-Fe, and Gel samples.

hydrogel due to the small amount of BiH NRs, the Gel-BiH-Alla hydrogel showed small peaks related to the crystalline structure of Alla.

Thermogravimetric analysis (TGA) demonstrated weight loss stages for FG, Alg, FeCl<sub>3</sub>·6H<sub>2</sub>O, FG-Fe, and Gel samples during the heating process (Fig. 3c). The required temperature for 10% and 50% weight loss and the final residual amount at 800 °C of each sample are presented in Fig. 3d. In the first step for all samples, a slight weight loss occurred below the temperature of 200–250 °C due to the loss of the absorbed moisture and other volatile products.<sup>76</sup> As for Alg, the second drop of weight started at 217 °C due to polymer degradation, which caused a 79.0% decomposition rate.<sup>77</sup> Moreover, above 232 °C the second and most remarkable weight loss of FG occurred due to polysaccharide degradation, which led to an 85.0% decomposition rate at 800 °C.<sup>18,78</sup> Furthermore, the second drop in the weight of FeCl<sub>3</sub>·6H<sub>2</sub>O commenced at 200 °C and this was ascribed to the dehydrochlorination process.<sup>79</sup> The weight loss stages of FG-Fe and Gel were similar to that of FG due to being the major component of the hydrogels, and their weight losses at 800 °C were 77.3% and 83.4%, respectively. Moreover, 50% weight losses of FG-Fe and Gel hydrogels occurred at 295 °C and 300 °C, respectively;

however, that occurred at 294 °C, 293 °C, and 157 °C for FG, Alg, and FeCl<sub>3</sub>·6H<sub>2</sub>O, respectively, indicating the higher thermal stability of hydrogels, which was due to the presence of metal-coordinated bonds. Meanwhile, derivative thermogravimetry (DTG) analysis was carried out based on the TGA results, which represent the weight loss rate against the temperature. Maximum decomposition speed for the Gel sample occurred with 0.59% °C<sup>-1</sup> at 261 °C, indicating the improved thermal stability of the hydrogel compared to pure ingredients due to metal-coordinated crosslinking (Fig. 3e).

**2.2.4. Morphological properties and EDAX studies of the hydrogels.** FE-SEM was performed under different magnifications to evaluate the surface morphology, which showed high porosity of freeze-dried Gel (Fig. 4a) and Gel-BiH (Fig. 4b) hydrogels that was in line with the obtained porosity values of the ethanol displacement method. The porous structure facilitates exudate collection, distribution of nutrients and oxygen in the wound environment, cell adhesion, and growth.<sup>80</sup> EDAX was used to determine the elemental content of the FG, FG-Fe, Gel, and Gel-BiH samples (Fig. 4c). The analysis of the extracted FG showed the presence of O (50.4%) and C (48.5%) elements. The analysis of FG-Fe, Gel, and Gel-BiH hydrogels showed the presence of the Fe element as well as O



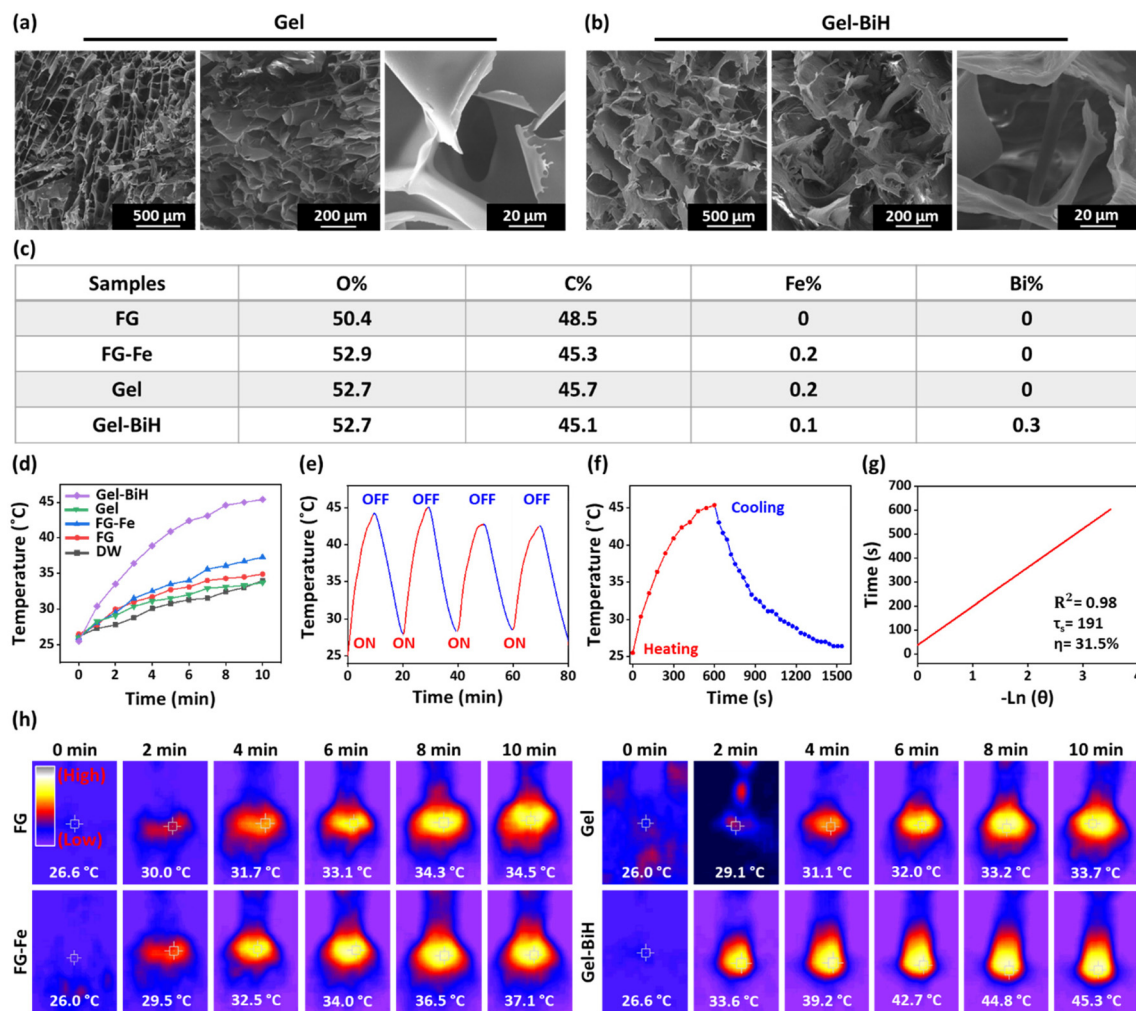


**Fig. 4** (a and b) FE-SEM images of Gel and Gel-BiH hydrogel with three different magnifications. (c) EDAX analyses of FG, FG-Fe, Gel, and Gel-BiH samples. (d) Photothermal temperature curves of DW, FG, FG-Fe, Gel, and Gel-BiH samples under 808 nm laser (1 W cm<sup>-2</sup>) irradiation for 10 min. (e) Temperature variations of Gel-BiH over four continuous ON/OFF cycles of 808 nm laser irradiation (1 W cm<sup>-2</sup>). (f) Photothermal responses of the Gel-BiH hydrogel upon laser irradiation (808 nm, 1 W cm<sup>-2</sup>) for 10 min and the cooling phase of 15 min. (g) The plot of cooling time versus the negative natural logarithm of the temperature driving force. The  $\eta$  value of Gel-BiH was calculated 31.5%. (h) Infrared photographs of FG, FG-Fe, Gel, and Gel-BiH samples during irradiation with an 808 nm laser for 10 min (1 W cm<sup>-2</sup>).

and C elements, corroborating the formation of Fe<sup>3+</sup>-coordinated bonds and effective crosslinking. Moreover, the EDAX analysis of the Gel-BiH hydrogel indicated the presence of the Bi element as compared to the Gel sample, confirming the successful loading of BiH NRs within the hydrogel.

**2.2.5. Photothermal effect of the hydrogel.** The *in vitro* photothermal effect of different formulations was assessed under 808 nm NIR irradiation with the power density of 1 W cm<sup>-2</sup> for 10 min (Fig. 4d). The temperature of the Gel-BiH hydrogel containing 200 μg ml<sup>-1</sup> of BiH NRs increased significantly to 45.4 °C, which was approximately close to the temperature of the BiH solution (200 μg ml<sup>-1</sup>) after laser irradiation (1 W cm<sup>-2</sup>, 10 min). However, there were no remarkable changes in the temperatures of DW, FG, FG-Fe, and Gel samples. Thermal images of different formulations under laser irradiation are shown in Fig. 4h. The Gel-BiH hydrogel

exhibited outstanding temperature stability after 4 repeating ON/OFF cycles of NIR irradiation, indicating the possibility of multiple PTTs after a single injection of the hydrogel (Fig. 4e). To evaluate the photothermal conversion efficiency ( $\eta$ ) of the BiH NRs, 1 ml of the Gel-BiH hydrogel was heated up under laser irradiation for 10 min (808 nm, 1 W cm<sup>-2</sup>) and then cooled down (Fig. 4f). The  $\eta$  value of BiH NRs was obtained as 31.5% (Fig. 4g) according to eqn (5) presented in section 1.5.6. of the ESI,<sup>†</sup> which was sufficient for good PTT performances.

**2.2.6. Rheological properties and injectability of the hydrogels.** Rheology can be used to determine the viscoelastic properties of injectable hydrogels in response to the applied stress. The viscosity of Gel (Fig. S5a<sup>†</sup>), Gel-BiH (Fig. S5b<sup>†</sup>), and Gel-BiH-Ala (Fig. S5c<sup>†</sup>) hydrogels decreased considerably with shear rate increment, confirming the shear-thinning property of all hydrogels, which is an important factor for





injectability.<sup>81,82</sup> Noticeably, the Gel sample showed a higher viscosity compared to the Gel-BiH hydrogel, which could be due to the less interaction of  $\text{Fe}^{3+}$  with the hydroxyl and carboxyl groups of FG and Alg in the presence of  $\text{Bi}^{3+}$  ions. The frequency sweep test analyzed the behavior of hydrogels in constant strain (0.1%) and variable frequencies from 0.1 to 100

$\text{rad s}^{-1}$ . The elastic behavior ( $G'$ ) of Gel (Fig. 5a) and Gel-BiH (Fig. 5d) hydrogels were superior to the viscous behavior ( $G''$ ), indicating the gel-like behavior of both hydrogels. The strain sweep test for both Gel (Fig. 5b) and Gel-BiH (Fig. 5e) hydrogels were conducted at a constant frequency (10  $\text{rad s}^{-1}$ ) using variable strains from 0.1 to 100%. The  $G'$  and  $G''$  curves of Gel

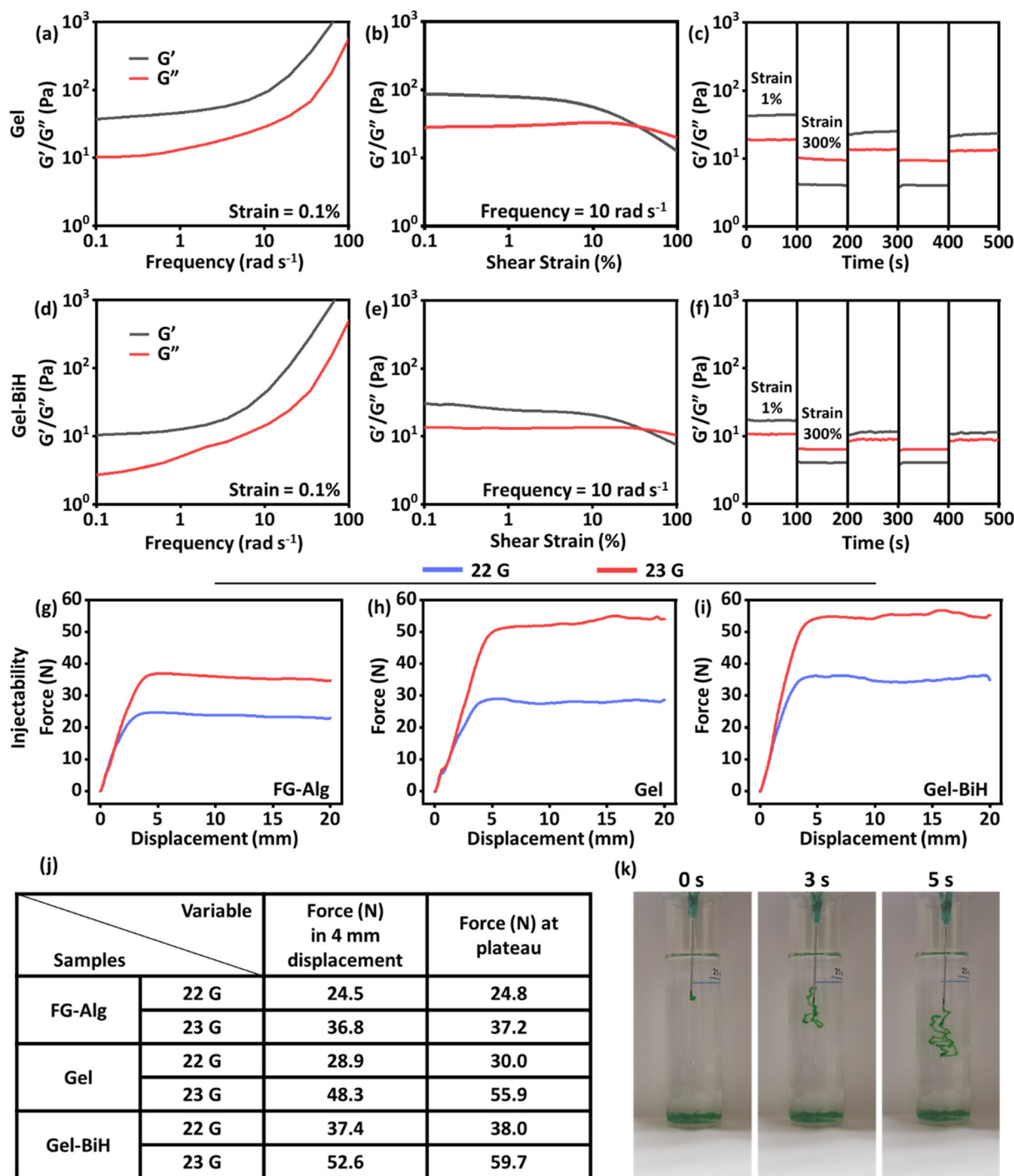


Fig. 5 Rheological properties of (a–c) Gel and (d–f) Gel-BiH samples. Injection force-displacement curves for (g) FG-Alg, (h) Gel, and (i) Gel-BiH injected from a 10 ml syringe using 22 and 23 G needles. (j) The force needed for 4 mm displacement and the maximum force in the plateau are presented for different samples using 22 G and 23 G needles. (k) Photographs of injectability of the colored Gel sample in DW over time.





and Gel-BiH hydrogels intersected at about 35% and 32%, respectively, which showed that the tolerated strain broke the hydrogel network. The results indicate a slightly less robust network of the Gel-BiH hydrogel compared to the Gel hydrogel due to the incorporation of BiH NRs. The higher  $G'$  value compared to  $G''$  before the intersection of curves indicated the elastic characteristic of the hydrogel; however, the higher  $G''$  value compared to  $G'$  after the intersection of curves demonstrated fluid-like characteristics of both hydrogels. The alternate-step strain study showed that Gel (Fig. 5c) and Gel-BiH (Fig. 5f) hydrogels could transform from a flexible material at high strains ( $G' < G''$ ) into a stiff material at low strains ( $G' > G''$ ) in continuous low (1%) and high (300%) strains at a frequency of  $10 \text{ rad s}^{-1}$ .<sup>82,83</sup> Moreover, the results demonstrated the quick recovery of  $G'$  and  $G''$  values in continuous strain fluctuations, revealing the desired self-healing properties due to the reversible nature of metal-coordinated crosslinks of Gel and Gel-BiH hydrogels.

The injectability of hydrogels has made them ideal formulations for application in the field of drug delivery and tissue engineering due to their low invasiveness and providing an adaptable shape after administration.<sup>84</sup> The injection force needed for the extrusion of a hydrogel is closely associated with its rheological properties, which was measured using a mechanical test at a steady speed rate of injection ( $60 \text{ mm min}^{-1}$ ) from a 10 ml syringe equipped with 22 gauge (G) and 23 G needles.<sup>85</sup> The force (N) against displacement (mm) was then plotted for FG-Alg, Gel, and Gel-BiH samples. The force required for the injection of FG-Alg at 4 mm of displacement was 24.5 N with a 22 G needle and 36.8 N using a 23 G needle (Fig. 5g). These values increased to 28.9 N and 48.3 N for Gel (Fig. 5h) and 37.4 N and 52.6 N for Gel-BiH hydrogel (Fig. 5i) using 22 and 23 G needles, respectively, due to the metal-coordinated bonds formed in the hydrogel as compared to the FG-Alg sample. There was no significant difference in the required injectability force for the ejection of Gel and Gel-BiH samples. Furthermore, as expected, the force needed to eject the hydrogels was higher by a needle with a narrow gauge (23 G) in all samples. The recorded force at 4 mm of displacement and the plateau phase are demonstrated for different samples with different needles (Fig. 5j). The injectability photographs of the green-colored Gel sample in DW are also shown over time in Fig. 5k. Taken together, we developed an injectable shear-thinning hydrogel than can be used for intratumoral injection or covering of the wound site.

### 2.3. *In vitro* biocompatibility assays

Hemocompatibility is one of the most important criteria for the *in vivo* application of biomaterials.<sup>86</sup> Therefore, *in vitro* hemolysis assay was performed to evaluate the hemocompatibility of different concentrations ( $1 \text{ mg ml}^{-1}$ ,  $2 \text{ mg ml}^{-1}$ , and  $3 \text{ mg ml}^{-1}$ ) of Gel, Gel-BiH, and Gel-BiH-Ala hydrogels at different time points. As shown in Fig. 6a, all hydrogels were classified as non-hemolytic biomaterials (non-hemolyzed RBCs >98%) based on the safe hemolysis index defined by ISO standards (<5%).<sup>87</sup> DW and phosphate-buffered saline (PBS,

pH 7.4) were used as positive and negative control groups, respectively. The corresponding hemolysis photographs of RBCs are shown in Fig. 6b. The transparency of the supernatant in all samples was similar to that of the negative control group (PBS) and the red color of the positive control (DW) was due to the complete lysis of RBCs.

Moreover, the *in vitro* cytotoxicity of Gel and Gel-BiH hydrogels ( $100 \mu\text{g ml}^{-1}$ ,  $200 \mu\text{g ml}^{-1}$ , and  $300 \mu\text{g ml}^{-1}$ ) were assessed on the 3T3 fibroblast cells after 24- and 48 h of incubation. No significant difference was observed in the cell viabilities of hydrogels compared to that of the control group at different concentrations and time points, due to the safe nature of polymers used as hydrogel matrixes (Fig. 6c and d). Notably, the Gel-BiH-Ala treated group exhibited a higher cell viability in comparison with that of the control group in all concentrations and time points (Fig. 6e). This outcome is associated with the cell growth-stimulating effect of Ala presented in the final formulation.<sup>36</sup> Consequently, the Gel-BiH-Ala hydrogel represented improved cytocompatibility, making it a promising candidate for biomedical applications.

### 2.4. *In vivo* toxicity

To assess *in vivo* toxicity, the histological analysis of the main organs of rats (kidneys, spleen, and liver) were carried out by hematoxylin & eosin (H&E) staining at day 14 after the subcutaneous injection of the Gel, Gel-BiH, and Gel-BiH-Ala hydrogels ( $500 \mu\text{l}$ ). No obvious abnormality, organelle damage, and inflammation were observed in different hydrogel-treated groups, demonstrating the desirable safety and histocompatibility of the formulations (Fig. 7a). Furthermore, the blood biochemical and hematological parameters were evaluated to confirm the biosafety of hydrogels. No significant difference was observed in hematological factors of hydrogel-treated groups, including the blood level of RBCs, hemoglobin (HGB), hematocrit (HCT), platelet (PLT), white blood cells (WBCs), neutrophils (NEUT), lymphocytes (LYMPH), and monocytes (MONO) as compared to that of the control group (Fig. 7b). Furthermore, biochemical indexes and minerals, including total protein (TP), albumin (ALB), calcium (Ca), phosphorus (Ph), blood urea nitrogen (BUN), creatinine (CREA), lactate dehydrogenase (LDH), and alkaline phosphatase (ALP) did not show any meaningful difference between all hydrogel-treated groups and the control (Fig. S6†).

### 2.5. *In vitro* and *in vivo* blood clotting studies

It is known that hemostatic hydrogels can control hemorrhage in the wound and accelerate the healing process.<sup>88</sup> Therefore, the *in vitro* blood clotting potentials of Gel, Gel-BiH, and Gel-BiH-Ala hydrogels were assessed using the blood clotting index (BCI), in which the lower value indicates the better clotting effect of a hydrogel.<sup>89</sup> As shown in Fig. 8a, Gel, Gel-BiH, and Gel-BiH-Ala hydrogels in the BCI test showed blood coagulation, while a partial blood clotting formation was observed in the gauze-treated group, and there was no blood clot in the control group. The results showed that all hydrogels had lower BCI than those of the gauze and control groups at



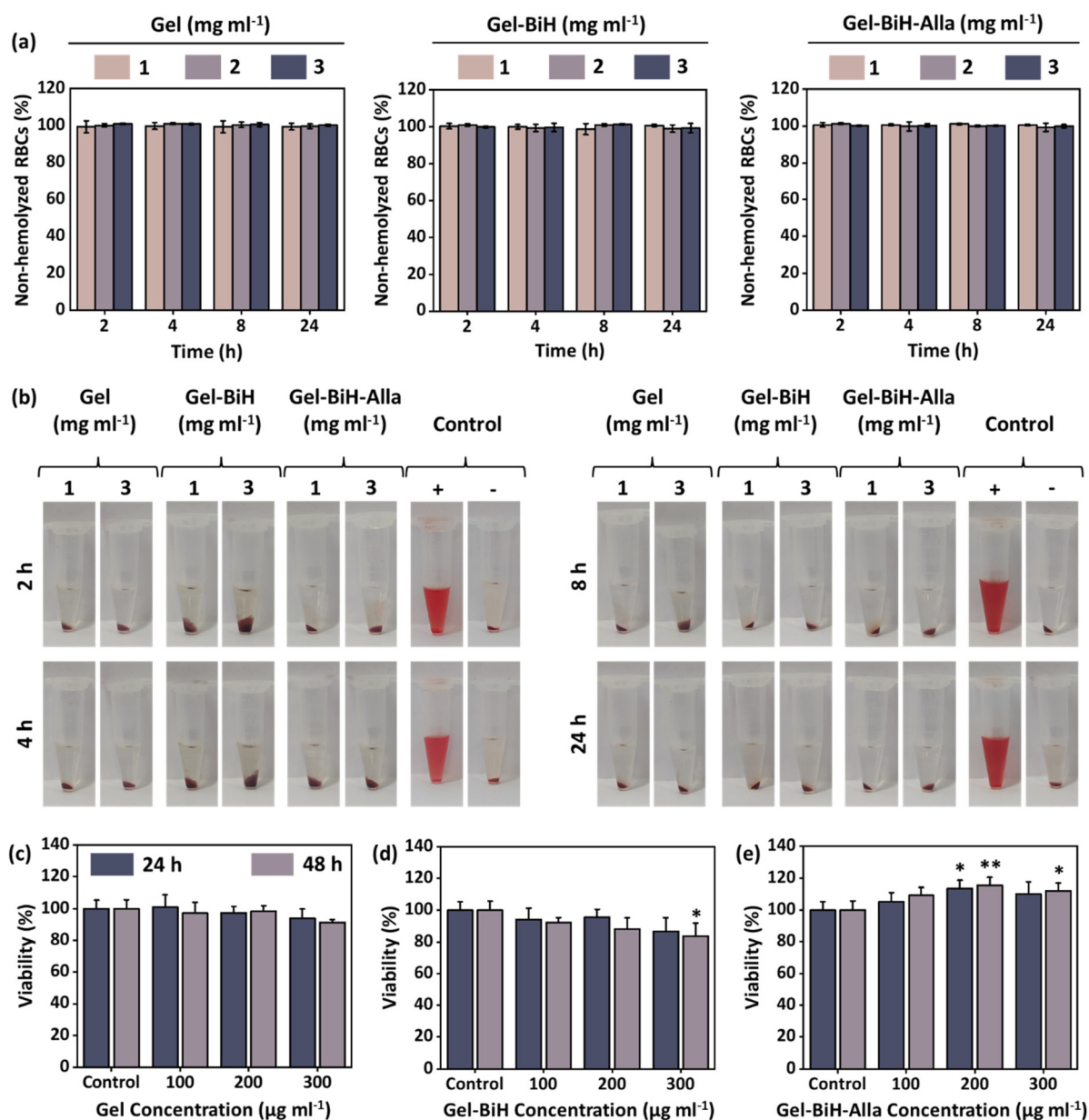


**Fig. 6** (a) Plots show the percentages of non-hemolyzed RBCs (%) after treatment with Gel, Gel-BiH, and Gel-BiH-Ala with the concentrations of 1, 2, and 3 mg ml<sup>-1</sup> after 2, 4, 8, and 24 h of co-incubation. (b) Photographs of centrifuged samples with different concentrations and time points. Viabilities of fibroblast cells after exposure to 100, 200, and 300 μg ml<sup>-1</sup> of (c) Gel, (d) Gel-BiH, and (e) Gel-BiH-Ala hydrogels incubated for 24 and 48 h at 37 °C, quantified by the CellTiter-Glo luminescence assay. Data are presented as the mean ± SD (*N* = 4). The data were statistically analyzed using one-way ANOVA (\**p* < 0.05, \*\**p* < 0.01) as compared with the control group.

different time points. BCI values were 22.8%, 24.7%, 24.2%, and 91.7% for Gel, Gel-BiH, Gel-BiH-Ala, and gauze samples, respectively, after incubation for 240 s (Fig. 8b), confirming the strong blood clotting effect of the hydrogels.

The rat tail-amputation model was also used to evaluate the *in vivo* hemostatic properties of hydrogels. The amount of blood loss was significantly reduced in Gel, Gel-BiH, and Gel-BiH-Ala treated groups compared to those in the control and gauze-treated groups (Fig. 8c). Besides, the tail-bleeding time was approximately 6 min for the gauze and control; however, it

was remarkably shortened to 32 ± 2 s, 40 ± 2 s, and 80 ± 21 s for Gel, Gel-BiH, and Gel-BiH-Ala hydrogels, respectively (Fig. 8c). Obviously, digital photographs of amputated tails showed that the amount of blood loss for hydrogel treated groups was significantly lower than those in the control and gauze-treated groups (Fig. 8d).

Both *in vitro* and *in vivo* evaluation of blood coagulation demonstrate the excellent and rapid hemostatic capacity of the prepared hydrogels, which can be due to three possible reasons:



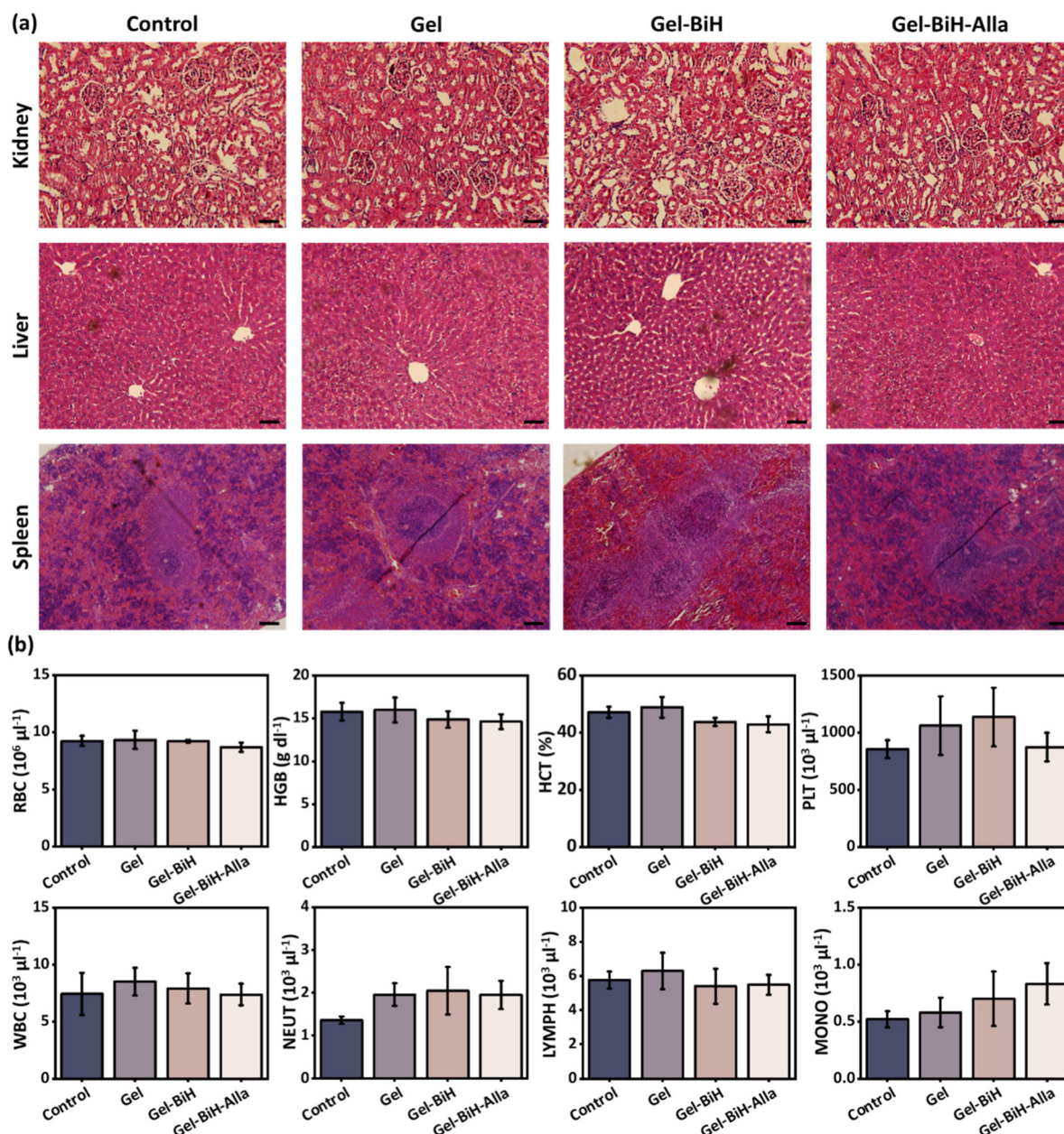


Fig. 7 *In vivo* toxicity study of the Gel, Gel-BiH, and Gel-BiH-Ala hydrogels. (a) H&E staining of kidneys, liver, and spleen of rats 14 days after the subcutaneous injection of normal saline as the control group and different hydrogels (500  $\mu$ l). Scale bar = 100  $\mu$ m. (b) Hematological factors of animals treated with hydrogels. Data are presented as the mean  $\pm$  SD ( $N = 3$ ).

The three-dimensional porous structure of the hydrogels promotes rapid and effective hemostasis.

The high-water absorbing capability of Alg and FG in the hydrogels enhances the hemostatic effect.<sup>19,90,91</sup>

Both Alg and FG are negatively charged biomaterials, which can stimulate the intrinsic pathway of the coagulation cascade via the activation of the coagulation factor XII.<sup>25,26</sup>

## 2.6. Antibacterial effect of the hydrogels

Microbial infections in cancer patients lead to disturbances in the treatment process and prolonged hospitalization.

Moreover, it also leads to an increased cost of health care and a reduced survival rate. Therefore, preparing an antibacterial hydrogel is of great significance in medicines, mainly when the treatment strategy of cancer is associated with the localized incidence of lesions.<sup>4,92,93</sup> *Staphylococcus aureus* (*S. aureus*), as Gram-positive bacteria, and *Escherichia coli* (*E. coli*), as Gram-negative bacteria, were used to evaluate the antibacterial effects of the prepared hydrogels with and without laser irradiation by the colony counting method. As shown in Fig. 8e, Gel-BiH and Gel-BiH-Ala hydrogels could eradicate most of the bacteria without NIR irradiation, which is related





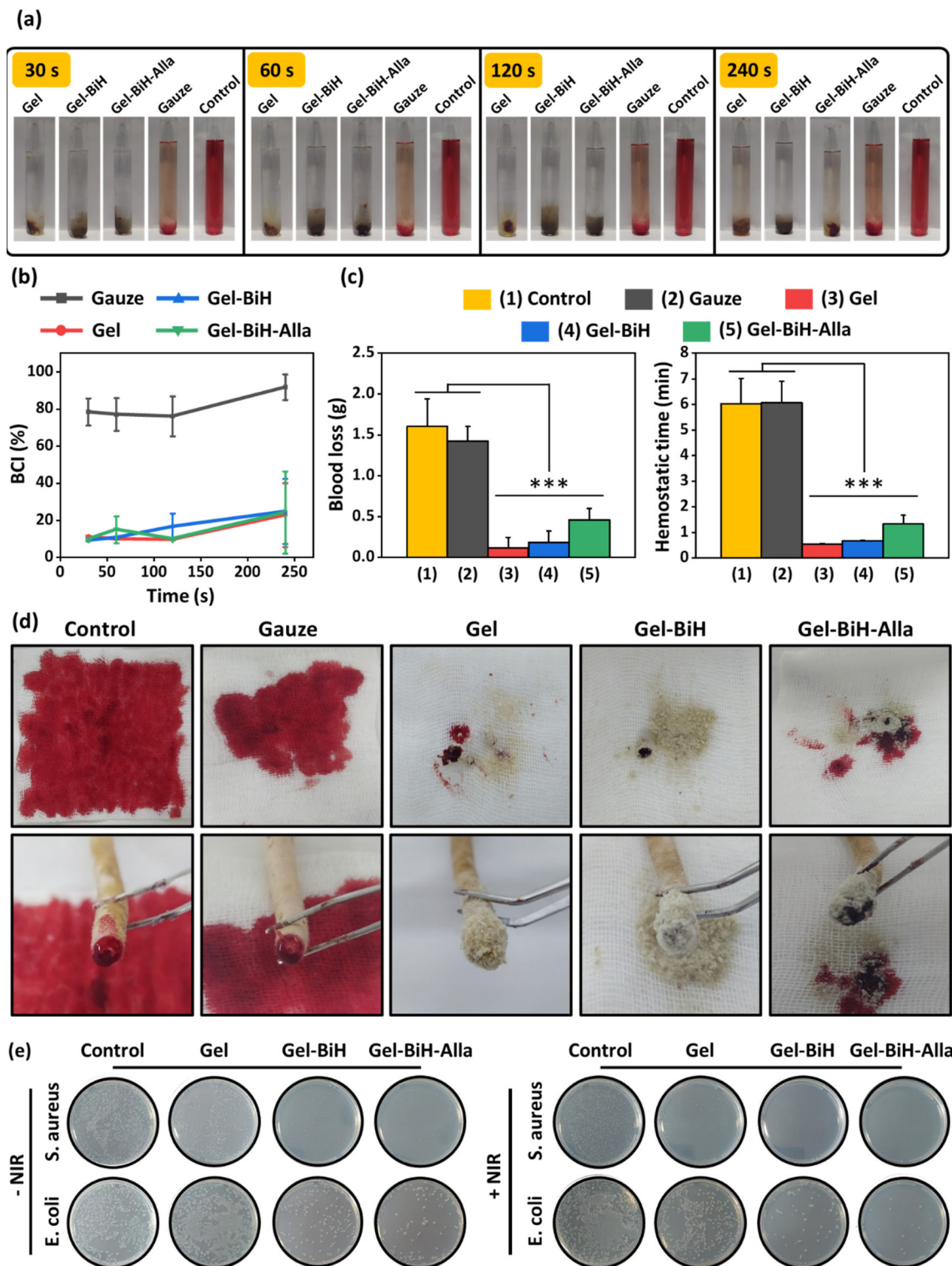


**Fig. 8** (a) Photographs of *in vitro* blood clotting effect of Gel, Gel-BiH, and Gel-BiH-Ala hydrogels, gauze, and control samples. (b) The dependence of blood clotting index (BCI) on time ( $N = 3$ ). (c) Blood loss and hemostasis time of Gel, Gel-BiH, Gel-BiH-Ala hydrogels, gauze-treated groups, and control sample in the tail amputation method. (d) Digital images of the amount of blood loss and amputated tail in Gel, Gel-BiH, Gel-BiH-Ala hydrogels, gauze-treated groups, and control sample. Data are presented as the mean  $\pm$  SD ( $N = 3$ ). The data were statistically analyzed using one-way ANOVA ( $***p < 0.001$ ) as compared with the control and gauze-treated groups. (e) Photographs of bacterial colonies on an agar plate for *E. coli* and *S. aureus* in the control group and Gel, Gel-BiH, and Gel-BiH-Ala treated groups with and without NIR irradiation after 24 h incubation.





to the antibacterial activity of BiH NRs and Alla. The probable antibacterial mechanism of BiH NRs is due to the release of  $\text{Bi}^{3+}$  ions, which disrupts cell metabolism and metabolic energy source *via* inhibiting the tricarboxylic acid cycle.<sup>55,94</sup> Moreover, Alla was shown to have direct antimicrobial effects.<sup>95</sup> Additionally, Gel-BiH and Gel-BiH-Alla hydrogels showed synergistically antibacterial effects upon laser irradiation due to photothermal-induced heat generation, which disrupts essential intracellular reactions of bacteria *via* protein/enzyme denaturation, membrane rupture, and irreversible bacterial destruction.<sup>56</sup> However, in the control and Gel groups, all bacteria samples showed normal growth either in the presence or absence of NIR irradiation. Therefore, the final prepared hydrogel with NIR irradiation exhibited the highest bactericidal effect due to the antibacterial effect of BiH NRs, Alla, and NIR-induced temperature increment.

### 2.7. *In vivo* evaluation of photothermal effect PTT-induced cancer ablation

The *in vivo* evaluation of the photothermal activity after the subcutaneous injection of the Gel-BiH hydrogel (100  $\mu\text{l}$ ) at the dorsal region of the BALB/c mice demonstrated that the hydrogel temperature reached 41.7  $^{\circ}\text{C}$ , 47.8  $^{\circ}\text{C}$ , and 50.3  $^{\circ}\text{C}$  under 10 min of laser irradiation with power densities of 0.65  $\text{W cm}^{-2}$ , 1  $\text{W cm}^{-2}$ , and 1.5  $\text{W cm}^{-2}$ , respectively (Fig. S7a and S7b†). Accordingly, *in vivo* PTT evaluations confirmed *in vitro* PTT studies, and demonstrated the marked and reproducible heating effects of the Gel-BiH hydrogel, which could be efficient for cancer treatment by high-temperature PTT and wound healing by mild PTT using different power densities.

The BiH-assisted PTT was evaluated for cancer treatment in 4T1 tumor-bearing female BALB/c mice following the intratumoral injection of PBS, Gel, and Gel-BiH samples with and without laser irradiation (Fig. 9a). The local temperature of the Gel-BiH treated mice under laser irradiation (1.5  $\text{W cm}^{-2}$ ) remained constant at 50  $^{\circ}\text{C}$  for 4 min in the tumor site, which was adequate for killing tumor cells. In fact, high-temperature PTT is favorable for effective tumor ablation by necrosis and cellular dysregulation.<sup>43</sup> The photographs of tumors on the first day of treatment with different formulations in the presence and absence of NIR irradiation are shown in Fig. 9b. Two days after treatment, the Gel-BiH treated group with laser irradiation showed a notable reduction (84%) in relative tumor volume, which could effectively eliminate tumor cells at the end of the study (Fig. 9c), due to BiH-induced heat generation. However, a time-dependent increase in tumor volumes of mice receiving treatment of Gel  $\pm$  NIR and Gel-BiH without NIR irradiation compared to PBS-treated groups was observed, due to nutrient supply by polymers employed in the hydrogels.

Additionally, there were no remarkable differences in the body weight of treated groups within 15 days (Fig. 9d). However, the body weight of the Gel-BiH + NIR treated group showed a slight reduction in the first 4 days, which could be a

result of decreased food intake due to the thermal injury and reduced tumor volume during treatment.

H&E-stained tumor tissues of the Gel-BiH + NIR treated group revealed a significant increase in tumor necrosis and incidence of cell membrane damage as well as loss of cell nuclei (Fig. 9e). Meanwhile, the histology analysis of PBS-treated groups with and without NIR irradiation demonstrated no necrotic or apoptotic cells. These results confirmed the effectiveness of BiH-mediated PTT in the complete ablation of tumor cells by minimal invasiveness.

### 2.8. *In vivo* wound healing study

Wound healing is a complex and dynamic process of regeneration of damaged tissue as closely as possible to its normal state.<sup>96</sup> Accordingly, the wound healing effect of the control group without any interference, Tegaderm<sup>TM</sup>, Gel, Gel-BiH  $\pm$  NIR, and Gel-BiH-Alla  $\pm$  NIR treated groups were evaluated by a full-thickness skin defect model. Tegaderm<sup>TM</sup>, Gel, Gel-BiH, and Gel-BiH-Alla hydrogels were applied to the created 18 mm skin defects (Fig. 10a). The strategy of PTT-induced mild hyperthermia was utilized and the temperature of Gel-BiH + NIR and Gel-BiH-Alla + NIR treated groups increased to 41.5  $^{\circ}\text{C}$  and 40  $^{\circ}\text{C}$  after 3 min of laser irradiation, respectively (Fig. 10b). To assess the wound closure rate, the wound site of different treated-groups was photographed on day 0, 3, 7, 10, and 14 (Fig. 10c). As shown in Fig. 10c and d, on the third day of treatment, the wound closure rate in Gel-BiH-Alla + NIR treated groups was approximately 12% higher compared to Tegaderm<sup>TM</sup> and Gel-BiH treated groups. Meanwhile, on the 10<sup>th</sup> day, the relative wound area for the Gel-BiH-Alla + NIR treated group was 5.8%; however, this value was 10.1% and 7.4% for Gel-BiH-Alla and Tegaderm<sup>TM</sup> treated groups, respectively, confirming the excellent wound healing effect of PTT. Moreover, at the end of the study it was found that, the relative wound area of the Gel-BiH-Alla + NIR treated group was smaller (0.39%) than that of the Gel-BiH-Alla (0.94%) and Tegaderm<sup>TM</sup> (0.96%) treated groups, presenting the outstanding effect of PTT-assisted multi-functional hydrogel in the wound healing process.

In addition, fourteen days after treatment, H&E staining of wound tissues exhibited a smaller amount of inflammatory cells infiltration and higher granulation tissue deposition in Gel-BiH and Gel-BiH-Alla treated groups with and without NIR irradiation, in comparison with the other groups (Fig. 10e). Gel-BiH-Alla + NIR treated wounds epithelialized faster contributing to swift wound closure; however, in the control and Tegaderm<sup>TM</sup> treated groups, re-epithelization occurred slowly just in peripheral regions of wounds. Moreover, the Gel-BiH-Alla + NIR treated group indicated the thinnest epidermal layer among the treated groups. In fact, at the final phase of the wound healing process, the epidermis reverted to the normal thickness, which was thickened after injury,<sup>97</sup> supporting the recovery of Gel-BiH-Alla + NIR treated wounds after a 14-day screening period. Additionally, repair of the epidermal layer also involved reconstruction of skin appen-



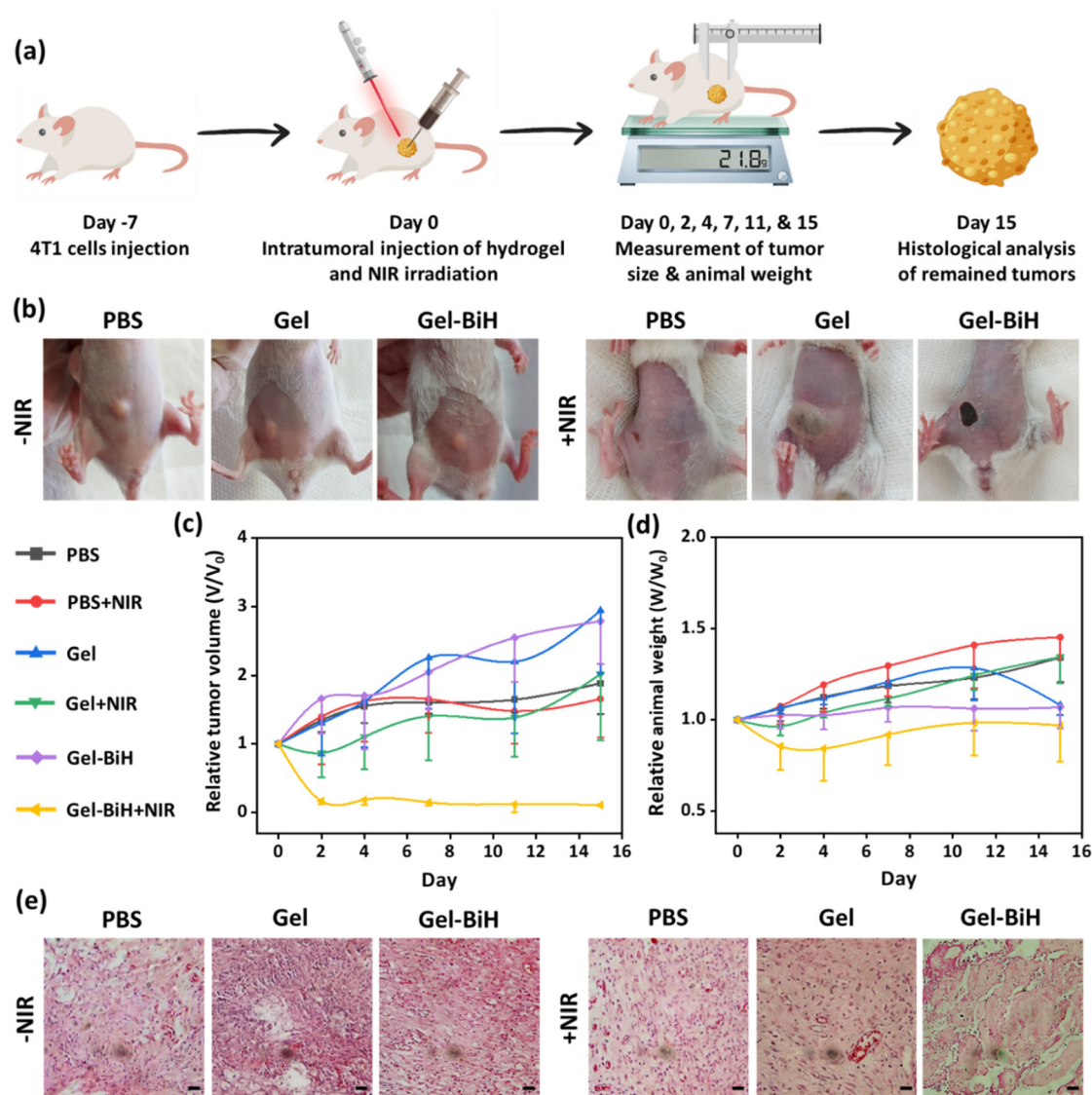


**Fig. 9** *In vivo* anti-cancer effect. (a) Schematic illustration of the method for PTT-mediated anti-cancer therapy. (b) Photographs of 4T1 tumor-bearing BALB/c mice treated with PBS, Gel, and Gel-BiH with or without 808 nm NIR laser irradiation with the power density of  $1.5 \text{ W cm}^{-2}$  on the first day of hydrogel injection. (c) Relative tumor volume and (d) relative animal weight in the mice over 15 days of treatment with different hydrogels in the presence and absence of NIR irradiation. (e) H&E-stained sections of tumor tissues after 15 days of treatment. Data are presented as the mean  $\pm$  SD ( $N = 5$ ). Scale bar = 100  $\mu\text{m}$ .

ages such as hair follicles and sebaceous glands, which were abundant in the Gel-BiH-Ala + NIR treated group. More importantly, H&E studies of the Gel-BiH-Ala  $\pm$  NIR treated groups showed the lowest blood vessel density with wound contraction, indicating the remodeling stage as the final phase of the wound healing process. However, abundant blood vessels were observed in other groups, representing the proliferative stage, which is the prior stage of the wound healing procedure.<sup>98</sup> According to Masson's trichrome staining, hydrogel-treated wounds with and without NIR irradiation showed higher deposition of collagen fibers compared to that with other groups, demonstrating a significant promoting effect on wound healing (Fig. 10f).

Taken together, the results obtained from wound healing studies represent that the Gel-BiH-Ala hydrogel can be injected into the wound area filling the wound in three dimensions, consequently improving skin regeneration and accelerating the wound healing process based on the release of the Ala and BiH-induced photothermal effect. Ala exhibits a tissue regeneration effect by facilitating the transition of a wound from the inflammatory state into the proliferative state, providing antibacterial effects and activating fibroblast proliferation.<sup>99,100</sup> Moreover, mild NIR light irradiation can promote endothelial cell proliferation, differentiation, and angiogenesis, and additionally enhance the anti-infection performance, resulting in excellent wound-healing efficiency.<sup>65</sup>





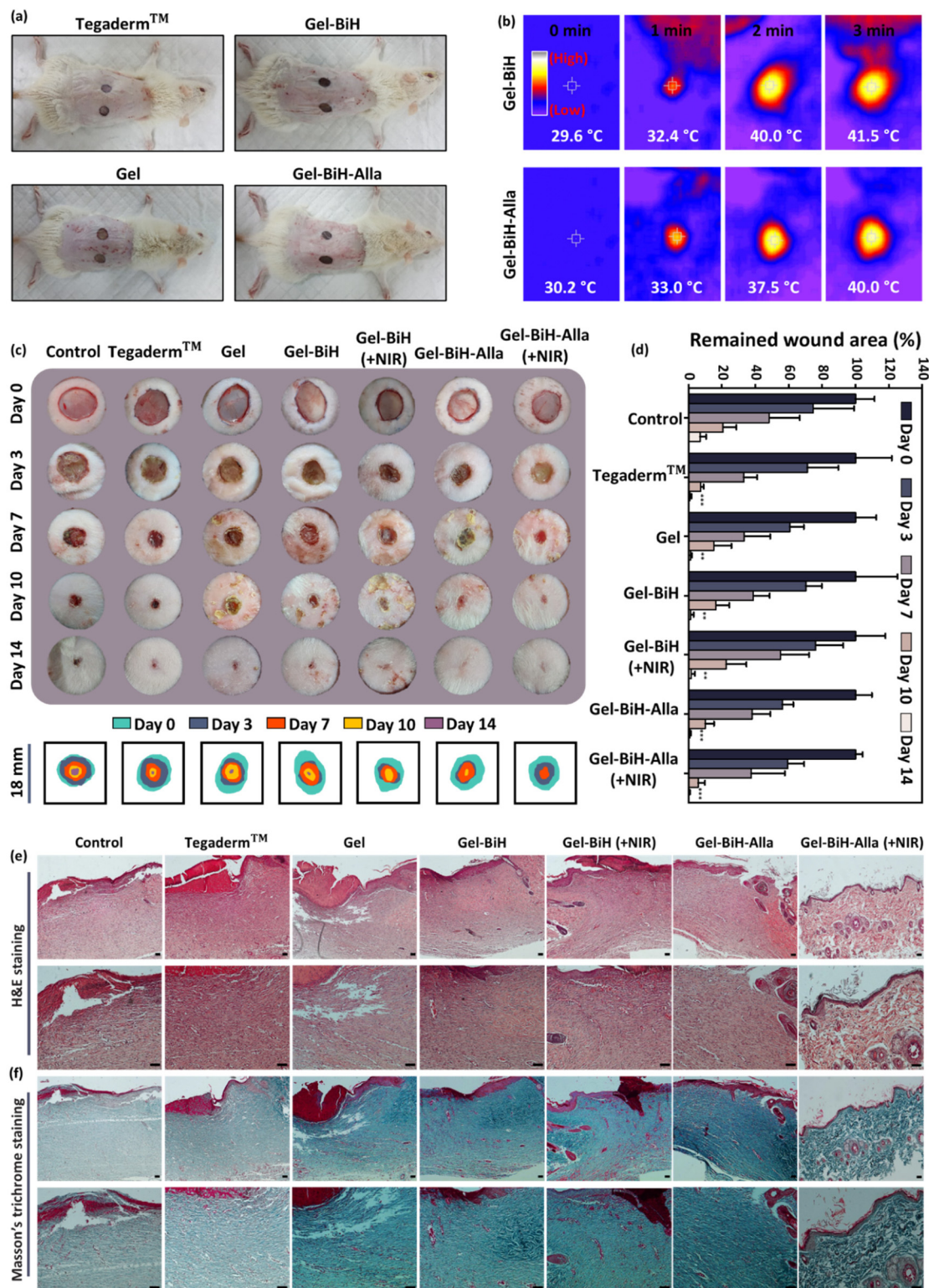


**Fig. 10** *In vivo* wound healing studies. (a) Photographs of full-thickness wounds in the dorsal region of rats treated with Tegaderm™, Gel, Gel-BiH, and Gel-BiH-Ala hydrogels on the first day of treatment. (b) Infrared thermal images of rats treated with Gel-BiH and Gel-BiH-Ala hydrogels exposed to an 808 nm NIR irradiation with the power density of 1 W cm<sup>-2</sup> for 3 min. (c) Skin photographs of wound closure in full-thickness wound model on days 0, 3, 7, 10, and 14 in the control group, Tegaderm™, Gel, Gel-BiH ± NIR, and Gel-BiH-Ala ± NIR treated groups (808 nm, 1 W cm<sup>-2</sup>, 3 min). Photographs were taken from a representative animal of each group. (Scale bar = 18 mm.) (d) The percentage of the remaining wound area for referred groups over 14 days of screening. Data are presented as the mean ± SD (N = 5). Statistical analysis was separately conducted for all groups compared to the control group using one-way ANOVA on the same day (\*\*p < 0.01, \*\*\*p < 0.001). (e and f) H&E and Masson's trichrome stained wound tissues in different groups on day 14 with different magnifications. Scale bar = 50 μm.



### 3. Conclusions

In summary, a photoactive injectable natural polymer-based hydrogel was developed with desirable biocompatibility for high-temperature ablation of tumors and mild temperature-based wound healing and infection control. The hydrogel was prepared *via* dynamic metal-coordination bonds, which provided desirable functionalities, including rapid gelation, self-healing, and injectable behaviors for therapeutics delivery with minimal invasiveness. Intratumoral injection of a BiH-embedded hydrogel upon laser irradiation demonstrated high-temperature-dependent killing of tumor cells. Moreover, the Gel-BiH-Ala hydrogel was applied directly over a wound bed followed by mild PTT, which increased the wound healing rate by the acceleration of re-epithelialization and collagen deposition due to the presence of Ala in the hydrogel matrix and mild hyperthermia. Furthermore, PTT-induced hyperthermia could eliminate infections due to the antibacterial activity of the loaded nanoparticles and heat generation. Concurrently, the porous structure of the hydrogel and its functionalities allowed rapid absorption of wound exudate, stopping hemorrhage, and promoting wound healing. Overall, this study offers a unique approach for treating various malignancies efficiently and overcoming cancer-related deaths using injectable hydrogels.

### Ethical statement

All animal procedures were performed in accordance with the Guidelines for Care and Use of Laboratory Animals of "Zanjan University of Medical Sciences" and approved by the Animal Ethics Committee of "Zanjan University of Medical Sciences" with the ethical code of IR.ZUMS.REC.1399.070.

### Conflicts of interest

There are no conflicts to declare.

### Acknowledgements

K. M. acknowledges the financial support from the School of Pharmacy, Zanjan University of Medical Sciences, Zanjan, Iran, under the framework of the thesis project (No. A-12-1296-7) with the ethical code of IR.ZUMS.REC.1399.070. Prof. M.-A. S. acknowledges the Iran National Science Foundation-National Natural Science Foundation of China joint grant (No. 4001987) and the Incentive fund from the University of Groningen.

### References

- 1 T. A. Buchholz, E. A. Mittendorf and K. K. Hunt, *JNCI Monogr.*, 2015, **2015**, 11–14.

- 2 M. Clarke, R. Collins, S. Darby, C. Davies, P. Elphinstone, V. Evans, J. Godwin, R. Gray, C. Hicks and S. James, *Lancet*, 2005, **366**, 2087–2106.
- 3 V. Shanmugam, S. Selvakumar and C.-S. Yeh, *Chem. Soc. Rev.*, 2014, **43**, 6254–6287.
- 4 H. Huang, X. Wang, W. Wang, X. Qu, X. Song, Y. Zhang, L. Zhong, D.-P. Yang, X. Dong and Y. Zhao, *Biomaterials*, 2022, **280**, 121289.
- 5 O. World Health, *WHO report on cancer: setting priorities, investing wisely and providing care for all*, World Health Organization, Geneva, Italy, 2020.
- 6 S. Lei, R. Zheng, S. Zhang, S. Wang, R. Chen, K. Sun, H. Zeng, J. Zhou and W. Wei, *Cancer Commun.*, 2021, **41**, 1183–1194.
- 7 Y. Tian, X. Jiang, X. Chen, Z. Shao and W. Yang, *Adv. Mater.*, 2014, **26**, 7393–7398.
- 8 L. Zhou, Y. Xi, Y. Xue, M. Wang, Y. Liu, Y. Guo and B. Lei, *Adv. Funct. Mater.*, 2019, **29**, 1806883.
- 9 H. Pan, R. Gray, J. Braybrooke, C. Davies, C. Taylor, P. McGale, R. Peto, K. I. Pritchard, J. Bergh and M. Dowsett, *N. Engl. J. Med.*, 2017, **377**, 1836–1846.
- 10 Y. Xi, J. Ge, M. Wang, M. Chen, W. Niu, W. Cheng, Y. Xue, C. Lin and B. Lei, *ACS Nano*, 2020, **14**, 2904–2916.
- 11 Y. Xi, J. Ge, Y. Guo, B. Lei and P. X. Ma, *ACS Nano*, 2018, **12**, 10772–10784.
- 12 M.-A. Shahbazi, L. Faghfour, M. P. Ferreira, P. Figueiredo, H. Maleki, F. Sefat, J. Hirvonen and H. A. Santos, *Chem. Soc. Rev.*, 2020, **49**, 1253–1321.
- 13 F. Poustchi, H. Amani, Z. Ahmadian, S. V. Niknezhad, S. Mehrabi, H. A. Santos and M. A. Shahbazi, *Adv. Healthcare Mater.*, 2021, **10**, 2001571.
- 14 H. He, L. Du, H. Xue, J. Wu and X. Shuai, *Acta Biomater.*, 2022, **149**, 297–306.
- 15 A. P. Mathew, S. Uthaman, K.-H. Cho, C.-S. Cho and I.-K. Park, *Int. J. Biol. Macromol.*, 2018, **110**, 17–29.
- 16 X. Xue, Y. Hu, Y. Deng and J. Su, *Adv. Funct. Mater.*, 2021, **31**, 2009432.
- 17 H. Molaei and K. Jahanbin, *Carbohydr. Polym.*, 2018, **182**, 98–105.
- 18 A. Amirsadeghi, A. Jafari, S.-S. Hashemi, A. Kazemi, Y. Ghasemi, A. Derakhshanfar, M.-A. Shahbazi and S. V. Niknezhad, *Mater. Today Commun.*, 2021, **27**, 102225.
- 19 M. Dabestani, R. Kakhodaee, G. O. Phillips and S. Abbasi, *Food Hydrocolloids*, 2018, **78**, 92–99.
- 20 F. Sadeghi, R. Kakhodaee, B. Emadzadeh and G. O. Phillips, *Carbohydr. Polym.*, 2018, **179**, 71–78.
- 21 A. Taheri and S. M. Jafari, *Adv. Colloid Interface Sci.*, 2019, **269**, 277–295.
- 22 P. Dehghani, S. M. H. Hosseini, M.-T. Golmakani, M. Majdinasab and S. Esteghlal, *Food Hydrocolloids*, 2018, **77**, 677–688.
- 23 C. J. Kastrup, M. Nahrendorf, J. L. Figueiredo, H. Lee, S. Kambhampati, T. Lee, S. W. Cho, R. Gorbato, Y. Iwamoto, T. T. Dang, P. Dutta, J. H. Yeon, H. Cheng, C. D. Pritchard, A. J. Vegas, C. D. Siegel, S. MacDougall, M. Okonkwo, A. Thai, J. R. Stone, A. J. Coury,





- R. Weissleder, R. Langer and D. G. Anderson, *Proc. Natl. Acad. Sci. U. S. A.*, 2012, **109**, 21444–21449.
- 24 C. Lee, J. Shin, J. S. Lee, E. Byun, J. H. Ryu, S. H. Um, D.-I. Kim, H. Lee and S.-W. Cho, *Biomacromolecules*, 2013, **14**, 2004–2013.
- 25 X. Yang, W. Liu, N. Li, M. Wang, B. Liang, I. Ullah, A. Luis Neve, Y. Feng, H. Chen and C. Shi, *Biomater. Sci.*, 2017, **5**, 2357–2368.
- 26 A. Golkar, S. M. Taghavi and F. Aghili Dehnavi, *Int. J. Food Prop.*, 2018, **21**, 416–436.
- 27 L. Shi, P. Ding, Y. Wang, Y. Zhang, D. Ossipov and J. Hilborn, *Macromol. Rapid Commun.*, 2019, **40**, 1800837.
- 28 H. Li, P. Yang, P. Pageni and C. Tang, *Macromol. Rapid Commun.*, 2017, **38**, 1700109.
- 29 H. S. Han and K. Y. Choi, *Biomedicines*, 2021, **9**, 305.
- 30 Y. Zhang, C. Zhu, Z. Zhang, J. Zhao, Y. Yuan and S. Wang, *Colloids Surf., B*, 2021, **207**, 112025.
- 31 X. Yuan, Y. Zhu, S. Li, Y. Wu, Z. Wang, R. Gao, S. Luo, J. Shen, J. Wu and L. Ge, *J. Nanobiotechnol.*, 2022, **20**, 154.
- 32 L. Luo, B. Qin, M. Jiang, L. Xie, Z. Luo, X. Guo, J. Zhang, X. Li, C. Zhu and Y. Du, *J. Nanobiotechnol.*, 2021, **19**, 1–18.
- 33 X. He, Y. Hao, B. Chu, Y. Yang, A. Sun, K. Shi, C. Yang, K. Zhou, Y. Qu and H. Li, *Nano Today*, 2021, **39**, 101174.
- 34 G. Gao, Y.-W. Jiang, Y. Guo, H.-R. Jia, X. Cheng, Y. Deng, X.-W. Yu, Y.-X. Zhu, H.-Y. Guo, W. Sun, X. Liu, J. Zhao, S. Yang, Z.-W. Yu, F. M. S. Raya, G. Liang and F.-G. Wu, *Adv. Funct. Mater.*, 2020, **30**, 1909391.
- 35 S. Liu, J. Yu, Q. Zhang, H. Lu, X. Qiu, D. Zhou, Y. Qi and Y. Huang, *Biomacromolecules*, 2020, **21**, 3795–3806.
- 36 Z. Ahmadian, A. Correia, M. Hasany, P. Figueiredo, F. Dobakhti, M. R. Eskandari, S. H. Hosseini, R. Abiri, S. Khorshid and J. Hirvonen, *Adv. Healthcare Mater.*, 2021, **10**, 2001122.
- 37 N. Asadi, H. Pazoki-Toroudi, A. R. Del Bakhshayesh, A. Akbarzadeh, S. Davaran and N. Annabi, *Int. J. Biol. Macromol.*, 2021, **170**, 728–750.
- 38 H. Chen, R. Cheng, X. Zhao, Y. Zhang, A. Tam, Y. Yan, H. Shen, Y. S. Zhang, J. Qi and Y. Feng, *NPG Asia Mater.*, 2019, **11**, 1–12.
- 39 G. Liu, Y. Zhou, Z. Xu, Z. Bao, L. Zheng and J. Wu, *Chin. Chem. Lett.*, 2022, **34**, 107705.
- 40 P. Xin, S. Han, J. Huang, X. You and J. Wu, *ACS Appl. Mater. Interfaces*, 2022, **14**, 34480–34487.
- 41 Z. Feng, Q. Su, C. Zhang, P. Huang, H. Song, A. Dong, D. Kong and W. Wang, *Adv. Funct. Mater.*, 2020, **30**, 2006454.
- 42 X. Qin, W. Qiao, Y. Wang, T. Li, X. Li, T. Gong, Z. R. Zhang and Y. Fu, *Macromol. Biosci.*, 2018, **18**, 1800047.
- 43 X. Yi, Q.-Y. Duan and F.-G. Wu, *Research*, 2021, **2021**, 9816594.
- 44 Y. Xu, H. Chen, Y. Fang and J. Wu, *Adv. Healthcare Mater.*, 2022, **11**, 2200494.
- 45 N. Behzadpour, N. Sattarahmady and N. Akbari, *J. Biomed. Phys. Eng.*, 2019, **9**, 661.
- 46 R. Lima-Sousa, D. de Melo-Diogo, C. G. Alves, C. S. Cabral, S. P. Miguel, A. G. Mendonça and I. J. Correia, *Mater. Sci. Eng., C*, 2020, **117**, 111294.
- 47 M. Liu, P. Huang, W. Wang, Z. Feng, J. Zhang, L. Deng and A. Dong, *J. Mater. Chem. B*, 2019, **7**, 2667–2677.
- 48 T. Chen, T. Yao, H. Pan, H. Peng, A. K. Whittaker, Y. Li, S. Zhu and Z. Wang, *Nano Res.*, 2022, **15**, 8636–8647.
- 49 B. Zhou, Y. Li, G. Niu, M. Lan, Q. Jia and Q. Liang, *ACS Appl. Mater. Interfaces*, 2016, **8**, 29899–29905.
- 50 R. Ouyang, P. Cao, P. Jia, H. Wang, T. Zong, C. Dai, J. Yuan, Y. Li, D. Sun and N. Guo, *Bioact. Mater.*, 2021, **6**, 386–403.
- 51 H. Guo, X. Zhao, H. Sun, H. Zhu and H. Sun, *Nanotechnology*, 2018, **30**, 075101.
- 52 Y. Zhu, Y. Wu, S. Li, X. Yuan, J. Shen, S. Luo, Z. Wang, R. Gao, J. Wu and L. Ge, *Chem. Eng. J.*, 2022, 137321.
- 53 D. S. Bhattacharya, D. Svehkarev, J. J. Soucek, T. K. Hill, M. A. Taylor, A. Natarajan and A. M. Mohs, *J. Mater. Chem. B*, 2017, **5**, 8183–8192.
- 54 C. Lei, X.-R. Liu, Q.-B. Chen, Y. Li, J.-L. Zhou, L.-Y. Zhou and T. Zou, *J. Controlled Release*, 2021, **331**, 416–433.
- 55 R. Vazquez-Munoz, M. J. Arellano-Jimenez and J. L. Lopez-Ribot, *BMC Biomed. Eng.*, 2020, **2**, 11.
- 56 Y. Chen, Y. Gao, Y. Chen, L. Liu, A. Mo and Q. Peng, *J. Controlled Release*, 2020, **328**, 251–262.
- 57 B. P. Lee, M.-H. Lin, A. Narkar, S. Konst and R. Wilharm, *Sens. Actuators, B*, 2015, **206**, 456–462.
- 58 L. Lu, T. Tian, S. Wu, T. Xiang and S. Zhou, *Polym. Chem.*, 2019, **10**, 1920–1929.
- 59 F. M. Al-Sogair, B. P. Opershall, A. Sigel, H. Sigel, J. Schnabl and R. K. O. Sigel, *Chem. Rev.*, 2011, **111**, 4964–5003.
- 60 G. C. Giri, S. Halder, G. Vijaykumar and M. Bera, *ChemistrySelect*, 2017, **2**, 2847–2857.
- 61 H. Ding, X. Liang, X. N. Zhang, Z. L. Wu, Z. Li and G. Sun, *Polymer*, 2019, **171**, 201–210.
- 62 N. Pazyar, R. Yaghoobi, E. Rafiee, A. Mehrabian and A. Feily, *Skin Pharmacol. Physiol.*, 2014, **27**, 303–310.
- 63 E. Saadat, N. Shakor, M. Gholami and F. A. Dorkoosh, *Int. J. Pharm.*, 2015, **489**, 218–225.
- 64 D. C. Onwudiwe and V. M. Nkwe, *Heliyon*, 2020, **6**, e04505.
- 65 X. Zhang, B. Tan, Y. Wu, M. Zhang and J. Liao, *Polymers*, 2021, **13**, 2100.
- 66 N. Masood, R. Ahmed, M. Tariq, Z. Ahmed, M. S. Masoud, I. Ali, R. Asghar, A. Andleeb and A. Hasan, *Int. J. Pharm.*, 2019, **559**, 23–36.
- 67 M. Rozenberg, S. Lansky, Y. Shoham and G. Shoham, *Spectrochim. Acta, Part A*, 2019, **222**, 116861.
- 68 G. Fadavi, M. A. Mohammadifar, A. Zargarraan, A. M. Mortazavian and R. Komeili, *Carbohydr. Polym.*, 2014, **101**, 1074–1080.
- 69 M. A. Inam, R. Khan, D. R. Park, Y.-W. Lee and I. T. Yeom, *Water*, 2018, **10**, 418.
- 70 S. R. Derkach, N. G. Voron'ko, N. I. Sokolan, D. S. Kolotova and Y. A. Kuchina, *J. Dispersion Sci. Technol.*, 2020, **41**, 690–698.



- 71 S. S. Imam, R. Adnan and N. H. Mohd Kaus, *Colloids Surf., A*, 2020, **585**, 124069.
- 72 M. Wang, L. Yang, J. Yuan, L. He, Y. Song, H. Zhang, Z. Zhang and S. Fang, *RSC Adv.*, 2018, **8**, 12459–12470.
- 73 M. J. Alam and S. Ahmad, *Spectrochim. Acta, Part A*, 2015, **136**, 961–978.
- 74 R. Bahari, Y. Shahbazi and N. Shavisi, *J. Food Sci.*, 2020, **85**, 3498–3508.
- 75 R. M. Nair, B. Bindhu and V. L. Reena, *J. Polym. Res.*, 2020, **27**, 154.
- 76 B. Kumar, R. Priyadarshi, Sauraj, F. Deeba, A. Kulshreshtha, K. K. Gaikwad, J. Kim, A. Kumar and Y. S. Negi, *Gels*, 2020, **6**, 49.
- 77 A. Salisu, M. M. Sanagi, A. Naim, K. J. Abd Karim, W. A. Wan Ibrahim and A. Umar, *Polym. Bull.*, 2015, **73**, 519–537.
- 78 S. Abbasi, in *Emerging Natural Hydrocolloids: Rheology and Functions*, ed. S. M. A. Razavi, Wiley-VCH, Weinheim, Germany, 2019, ch. 11, pp. 273–298.
- 79 S. Kanungo and S. Mishra, *J. Therm. Anal. Calorim.*, 1997, **48**, 385–401.
- 80 M. T. Khorasani, A. Joorabloo, A. Moghaddam, H. Shamsi and Z. MansooriMoghaddam, *Int. J. Biol. Macromol.*, 2018, **114**, 1203–1215.
- 81 S. Wang, H. Zheng, L. Zhou, F. Cheng, Z. Liu, H. Zhang and Q. Zhang, *Biomaterials*, 2020, **260**, 120314.
- 82 M. H. Chen, L. L. Wang, J. J. Chung, Y.-H. Kim, P. Atluri and J. A. Burdick, *ACS Biomater. Sci. Eng.*, 2017, **3**, 3146–3160.
- 83 X. Zhao, Y. Liang, Y. Huang, J. He, Y. Han and B. Guo, *Adv. Funct. Mater.*, 2020, **30**, 1910748.
- 84 Y. Sun, D. Nan, H. Jin and X. Qu, *Polym. Test.*, 2020, **81**, 106283.
- 85 T. E. Robinson, E. A. Hughes, N. M. Eisenstein, L. M. Grover and S. C. Cox, *J. Visualized Exp.*, 2020, e61417.
- 86 M. Weber, H. Steinle, S. Golombek, L. Hann, C. Schlensak, H. P. Wendel and M. Avci-Adali, *Front. Bioeng. Biotechnol.*, 2018, **6**, 99.
- 87 Y. Hu, Z. Zhang, Y. Li, X. Ding, D. Li, C. Shen and F.-J. Xu, *Macromol. Rapid Commun.*, 2018, **39**, 1800069.
- 88 Y. Liang, X. Zhao, T. Hu, B. Chen, Z. Yin, P. X. Ma and B. Guo, *Small*, 2019, **15**, 1900046.
- 89 L. Fan, H. Yang, J. Yang, M. Peng and J. Hu, *Carbohydr. Polym.*, 2016, **146**, 427–434.
- 90 H. Hattori, Y. Amano, Y. Nogami, B. Takase and M. Ishihara, *Ann. Biomed. Eng.*, 2010, **38**, 3724–3732.
- 91 C. Lv, L. Li, Z. Jiao, H. Yan, Z. Wang, Z. Wu, M. Guo, Y. Wang and P. Zhang, *Bioact. Mater.*, 2021, **6**, 2346–2359.
- 92 X. Fang, C. Wang, S. Zhou, P. Cui, H. Hu, X. Ni, P. Jiang and J. Wang, *Gels*, 2022, **8**, 315.
- 93 J. Rao, Y. Yang, H. Pan Bei, C.-Y. Tang and X. Zhao, *Biomater. Sci.*, 2020, **8**, 6814–6824.
- 94 Z. Chen, Q. Zhou and R. Ge, *BioMetals*, 2012, **25**, 95–102.
- 95 Y. D. Nokoorani, A. Shamloo, M. Bahadoran and H. Moravvej, *Sci. Rep.*, 2021, **11**, 1–20.
- 96 S. Dhivya, V. V. Padma and E. Santhini, *Biomedicine*, 2015, **5**, 1–5.
- 97 M. Arai, T. Matsuzaki and S. Ihara, *CellBio*, 2013, **2**, 248.
- 98 J. Li, J. Chen and R. Kirsner, *Clin. Dermatol.*, 2007, **25**, 9–18.
- 99 L. U. Araújo, A. Grabe-Guimarães, V. C. F. Mosqueira, C. M. Carneiro and N. M. Silva-Barcellos, *Acta Cir. Bras.*, 2010, **25**, 460–461.
- 100 Z. Bagheri, A. Azizi, K. Oshvandi, Y. Mohammadi and A. Larki-Harchegani, *J. Pharmacopunct.*, 2021, **24**, 196–205.

